JOURNAL OF MATERIALS SCIENCE 26 (1991) 6249 6259

Modes of deformation in rubber-modified thermoplastics during tensile impact

R. A. BUBECK
The Dow Chemical Company, Materials Science and Development Laboratory, 1702 Building, Midland, MI 48674, USA

D. J. BUCKLEY, Jr., E. J. KRAMER
Department of Materials Science and Engineering and the Materials Science Center, Bard Hall, Cornell University, Ithaca, NY 14853, USA

H. R. BROWN
IBM Research Division, Almaden Research Center, 650 Harry Road, San Jose, CA 95120, USA

Real-time small-angle X-ray scattering (RTSAXS) studies were performed on a series of rubber-modified thermoplastics. Scattering patterns were measured at successive time intervals as short as 1.8 ms and were analysed to determine the plastic strain due to crazing. Simultaneous measurements of the absorption of the primary beam by the sample allowed the total plastic strain to be computed. The plastic strain due to other deformation mechanisms, e.g. particle cavitation and macroscopic shear deformation was determined by the difference. Samples of commercial thicknesses can be studied at high rates of deformation without the inherent limitations of microscopy and its requirement of thin samples (i.e., plane strain constraint is maintained on sample morphology).

Contrary to the conclusions drawn from many previous dilatation-based studies, it has been demonstrated that the strain due to non-crazing mechanisms, such as rubber particle cavitation, and deformation of the glassy ligaments between rubber particles, occurs before that due to crazing mechanisms. Crazing accounts for at most only half of the total plastic strain in HIPS (high impact polystyrene) and ABS (rubber-modified styrene–acrylonitrile copolymer) materials. The proportion of strain attributable to crazing can be much less than half the total in thermoplastic systems with considerable shear yield during plastic deformation.

The predominant deformation mechanism in polycarbonate–ABS blends is shear in the PC (polycarbonate) with associated rubber gel particle cavitation in the ABS. This cavitation means that there appears to be a direct relationship between gel particle rubber content in the ABS and toughness of the blend. The mechanism is the same whether the tensile stress is in the direction parallel or perpendicular to the injection-moulded orientation, with simply less total strain being reached before fracture in the weaker perpendicular direction. Crazing, although the precursor to final fracture, occurs after the predominant mechanism and contributes only a few per cent to the total plastic deformation.

1. Introduction

The study of plastic deformation of polymers, and materials in general, has often included: (1) examination of the microstructure, (2) deformation of the specimen to the point of fracture, and (3) a post-mortem morphological analysis. Although the sequence of deformation events can be determined sometimes by microscopy, microscopy cannot yield the relative contribution of each deformation mode to the total plastic deformation as a function of time cannot. Applying the technique of real-time small angle X-ray scattering (RTSAXS), as recently reported in a preliminary fashion [1, 2], to the study of relatively high strain rate deformation opens the way to the direct observation of changes in X-ray scattering associated with the modes of deformation.

The principal means applied to the study of deformation of rubber-modified polymers in real time has been quantitative volumetric strain measurements, as practiced by Bucknall and coworkers [3–15], and by Maxwell and Yee [16]. These studies include: creep of high impact polystyrene (HIPS) [3, 5, 16], rubber-modified styrene–acrylonitrile copolymers (ABS) [4], ABS containing glass beads [6], rubber-modified polypropylene [8], and rubber-modified polymethylmethacrylate [9]. From these

0022–2461/91 $03.00 + .12

measurements the kinetics of craze formation and multiplication during deformation are usually inferred, although a weakness in the technique is its inability to discern crazing from other possible cavitation processes. Indeed, virtually all of the dilation in these studies is attributed to crazing alone. Breuer and coworkers [25] performed laser light scattering studies of thin ABS samples during tensile deformation. They showed that rubber particle cavitation associated with localized shear banding preceded crazing in the samples studied. Similar results for some ABS resins have also been observed using laser light scattering [26] by one of the authors. In a study involving stress sequences over relatively long times, Sue and Yee have utilized a double-edge-notch fracture specimen and post-mortem optical microscopy to study the deformation of nylon 6,6–polyphenylene oxide blends [22]. By examining the deformation zone extending from a slit notch that did not lead to fracture, they claimed that crazing precedes shear yield in the blend.

The combined RTSAXS mass thickness technique for studying deformation addresses some of the weaknesses associated with the techniques discussed above by often permitting: (1) the observation of the sequence of deformation events and (2) the discrimination between crazing and other larger scale cavitation processes under controlled deformation rates. Video-based data acquisition of RTSAXS patterns obtained during deformation has been used to determine that the impact behaviour of HIPS is governed primarily by the volume of craze matter generated and not by any changes in overall craze microstructure [1]. Similar studies have also shown that shear yielding can precede crazing in some ABS resins and, because of this, craze volume alone cannot account for the overall toughness of such materials. Recent refinements of the RTSAXS technique, in which a Reticon diode array detector has been substituted for a video-based pattern acquisition system [20], permits one to determine quantitatively the plastic strain due to crazing and due to non-crazing processes as a function of time. The application of this refined technique to the high strain rate deformation behaviour of HIPS, ABS, and PC–ABS (polycarbonate–ABS) blends is the principal topic of this paper.

2. Experimental procedure

2.1. Experimental techniques

The general experimental set-up, as assembled in the A-1 X-ray hutch at the Cornell High Energy Synchrotron Source (CHESS), is shown as a simplified schematic in Fig. 1. Samples were deformed in a tensile impact mode using a small hydraulic tensile fixture, fitted with a load cell and displacement indicator. The frame was mounted on an undercarriage which was translated perpendicular to the X-ray beam by two stepping motors so that the area of maximum stress on the specimen was in the X-ray beam at the moment of deformation and fracture. Optical video images of mounted samples taken using a fibre optic probe coupled to a TV camera aided the alignment process, as previously reported [1].

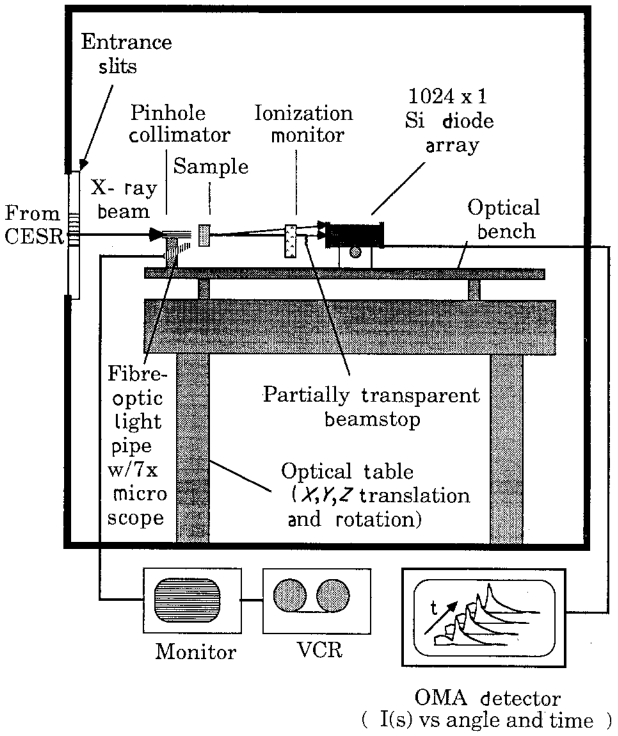

Figure 1 Schematic diagram of the experimental set-up.

Monochromatic 8 keV X-rays (wavelength $\lambda = 0.156$ nm) from the wiggler magnet with an approximate intensity of 1×10^{12} photons mm^{-2} s^{-1} were collimated with a 300 μm pinhole collimator. This arrangement yielded a beam intensity of approximately 10^{10} photons s^{-1} on the specimen as determined using a nitrogen gas-filled ionization monitor.

The data acquisition system used to obtain the SAXS patterns is based on a Princeton Applied Research optical multichannel analyser (OMA) equipped with a linear 1024-element X-ray sensitive Reticon diode array. The OMA records a one-dimensional X-ray scattering pattern with software-determined time resolution and angular spread. Time resolution is variable from milliseconds to hours while scanning the region between 2 and 20 milliradians from the primary beam. This range corresponds to microstructures of 9 to 90 nm in size at the wavelength of X-rays used. The detector has a relatively high dynamic range (16,800), thus permitting acquisition of scattering patterns from tensile impact samples without the saturation and phosphor lag problems associated with video detectors, such as those used in previous experiments [1, 2].

The SAXS pattern resulting from the scattering of X-rays from crazes is in the form of a cross through the origin [18, 19]. One arm of the cross is the result of scattering from craze fibrils whose axes are roughly perpendicular to that arm of the cross. The other arm of the cross-shaped pattern is due to the total external reflection from the interfaces of the crazes with the bulk polymer. While the intensity in the reflection streak is related to the area of these interfaces and their orientation, the intensity in the fibril scattering streak is proportional to the volume of craze matter

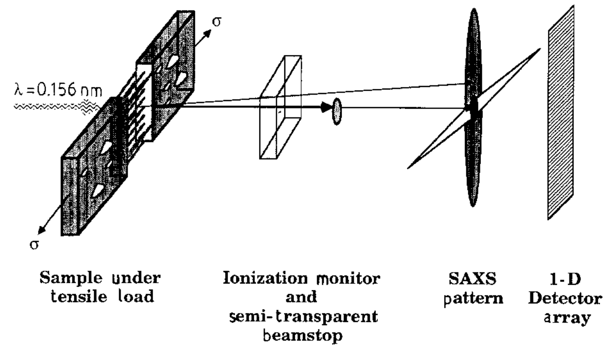

Figure 2 Experimental scattering geometry.

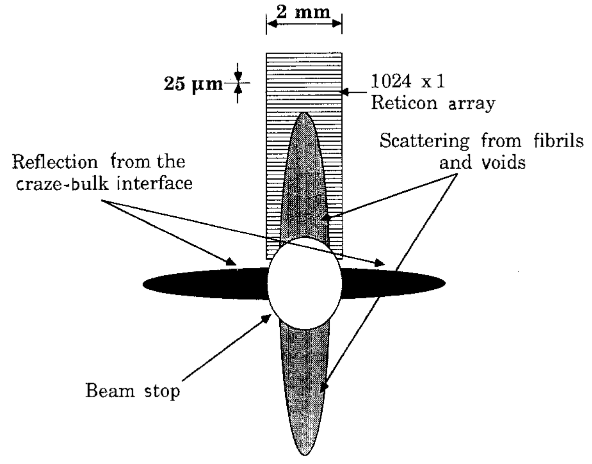

Figure 3 "Ideal" scattering pattern projected onto the Reticon detector array.

created in the X-ray beam, as discussed by Parades and Fischer [18] and Brown and Kramer [19]. A schematic diagram of the scattering geometry is shown in Fig. 2. As previously discussed, the ideal SAXS pattern from a bundle of vertically aligned crazes is in the form of a cross with the vertical scattering streak being due to the scattering from the craze fibrils. This vertical streak is projected upon, and recorded by the Reticon array, as shown in Fig. 3. About 30 to 70 pixels of the array are typically used.

Simultaneously with the measurement of the SAXS pattern, the intensity of the transmitted X-ray beam (as attenuated by the sample) was measured. This measurement was done either with an ionization monitor, as shown in Fig. 1, or by using a beam stop thinned over a small area so that a fraction of the transmitted beam intensity was recorded on a few elements of the Reticon detector. Real-time measurement of the transmitted X-ray beam intensity permitted the measurement of changes in the mass thickness, and thus the total plastic deformation of the sample weighted over the area of the X-ray beam. The changes in both transmitted and scattered intensities, as detected by the Reticon, are recorded and displayed by the OMA. A typical example is shown in Fig. 4 for an impact test of HIPS Styron* 484 at about 4.2 cm s^{-1}. The time resolution between scans is about 18.2 ms. Increases in main beam intensity beyond the sample due to decreases in mass absorption associated with sample deformation, as detected by pixels 2 to 7, yields the total strain due to all plastic deformation mechanisms (ε_T). The scattered intensity, as detected by pixels 16 to 65, can be analysed to find the strain due to crazing (ε_{CR}). A sharp jump in transmitted beam intensity is recorded coinciding with the cessation of craze fibril scattering and sample fracture. At any scan (time) the strain due to non-crazing processes (e.g., shear banding, rubber particle cavitation) can be obtained by subtracting ε_{CR} from ε_T. The analytical process by which these strains are computed is discussed in much more detail in Section 2.3, and by Buckley *et al.* [20].

2.2. Samples

Two high impact polystyrenes were studied (HIPS-1 and HIPS-2) each containing 7.5 wt % butadiene rubber in the form of gel particles (i.e., "composite" rubber particles with polystyrene inclusions) as generated by mass polymerization [21]. The average particle diameters were 2.8 and 1.2 μm, respectively, for HIPS 1 and 2. The weight average molecular weights of the polystyrene matrix for both was about 240 000 with a polydispersity of 2.8. Other than a minimal amount of antioxidant, no other additives were present in the resins.

The two ABS resins studied (ABS-1 and ABS-2) both had about a 2 μm average gel particle size, a 25 wt % acrylonitrile–polystyrene copolymer matrix of 150 000 weight average molecular weight, and a matrix polydispersity of 2.7. ABS-1 and ABS-2 have butadiene rubber contents of 10 and 22 wt %, respectively. Both samples contain about 1.5 wt % mineral oil.

Two polycarbonate–ABS blends (PC–ABS-1 and PC–ABS-2), each containing 35 wt % ABS, were included in this work. The bisphenol-A polycarbonate has a weight average molecular weight of 30 000.

The HIPS and ABS samples were compression moulded into 2 mm thick plaques, which were then machined into tensile specimens of dimensions 64 × 13 mm^2. Two circular stress concentrators with a radius of 6.35 mm were machined opposite to each other into the middle of each sample so as to provide a reduced tensile section with a 2 × 3 mm^2 cross-sectional area. In the case of the PC–ABS blends, 76 × 127 mm^2 plaques were injection moulded to simulate the oriented state in which this type of material is found in engineering applications. An important portion of the toughness of the blends is derived from the orientation induced by processing. Specimens were prepared so as to have an orientation axis perpendicular and parallel to the tensile axis.

2.3. Data analysis

The schema for analysis of the data involves the following steps: (1) the determination of total plastic strain ε_T from the decrease in X-ray absorption resulting from the sample decreasing in thickness

---

* Trademark of The Dow Chemical Company.

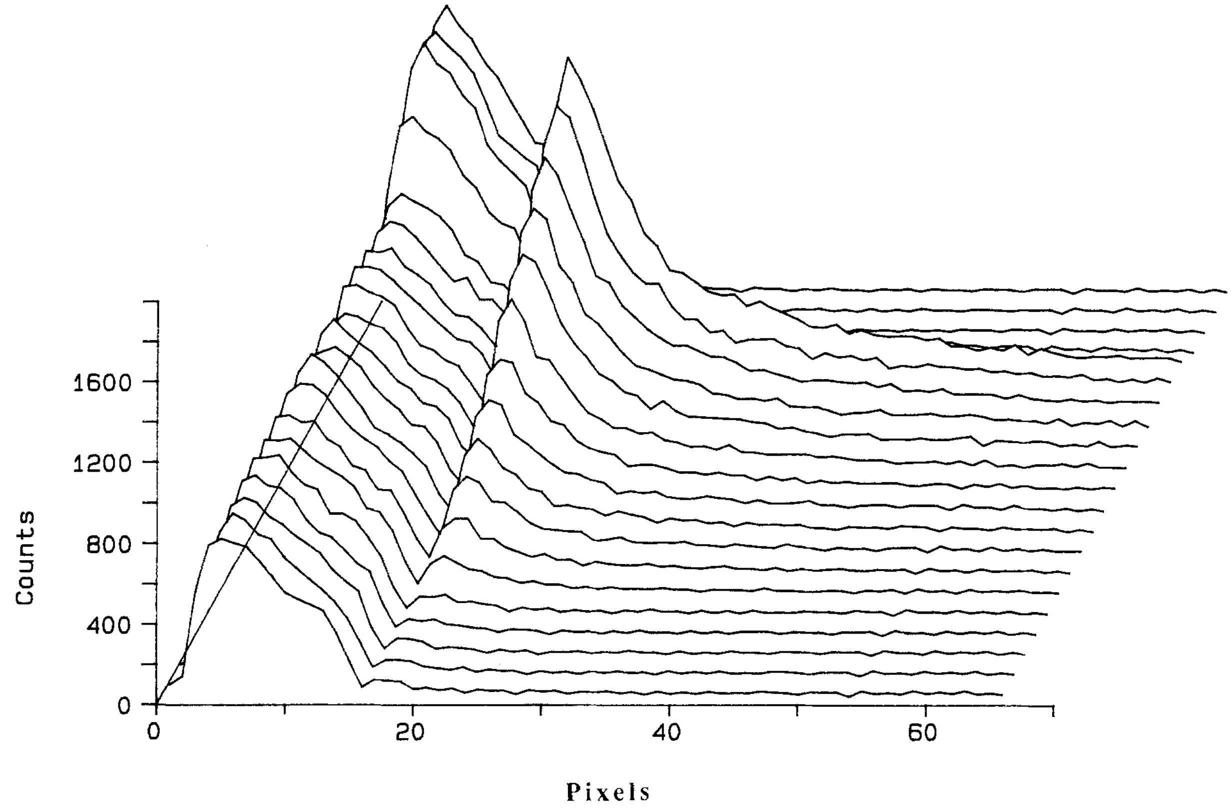

Figure 4 An example of line-summed intensities for RTSAXS during tensile impact of Styron 484 HIPS at a deformation rate of 4.2 cm s^{-1}. Time resolution is 18.2 ms scan^{-1}.

and/or developing internal cavities as a consequence of deformation; (2) calculating the plastic strain due to crazing ε_{CR} from the analysis of the absolute scattering invariant Q(Abs.) resulting from the scattering from the craze fibrils; and (3) the subtraction of ε_{CR} from ε_T to obtain the plastic strain due to non-crazing mechanisms (i.e., shear yielding, particle cavitation, etc.). The determination of Q(Abs.) requires the calibration of the scattering experiment with a standard such as a Lupolen polyethylene scattering standard in conjunction with a nitrogen gas primary beam ionization monitor. Once Q is of sufficient magnitude, information on the evolution of the craze microstructure can be estimated from each scattering curve. A more detailed explanation of the calculation sequence is contained in the following paragraphs of this section; additional details are also to be found in [20].

The change in sample mass thickness parameter* $\mu_s w_s$ and, hence ε_T, is calculated from the change in absorption as a function of time. At any instant, μw is equal to the mass thickness multiplied by the atomic mass absorption coefficient. The initial mass thickness parameter of the sample is determined using,

$$\mu_i w_i = \ln \frac{I_a}{I_o} \qquad (1)$$

where w_i is the initial sample thickness in the direction of the beam (usually about 2 mm), I_o is the main beam intensity monitored with the sample in place and before crazing, and I_a is the main beam intensity after the sample has been broken. The effective sample thickness (including thinning and all internal cavitation) is then easily estimated by monitoring the main beam intensity, I', behind the sample as a function of time, viz.,

$$\mu_s w_s = \ln \frac{I_a}{I'} \qquad (2)$$

Defining the extension ratios in the tensile and sample width (perpendicular to both the tensile and X-ray beam) directions, respectively, as Λ_1 and Λ_2, one can derive that the total plastic strain using conservation of mass in the gauge length, viz.

$$\Lambda_1 \Lambda_2 = \frac{\mu_i w_i}{\mu_s w_s}. \qquad (3)$$

(The extension ratio in the direction of the X-ray beam, Λ_3, will be utilized later.) The total plastic strain is expressed as,

$$\varepsilon_T = \ln(\Lambda_1) = \ln\left\{\frac{\mu_i w_i}{\mu_s w_s} \times \frac{1}{\Lambda_2}\right\} \qquad (4)$$

The true strain rates reported in this study are computed from the maximum slope of the plots of ε_T versus time. For many rubber-toughened polymers, e.g., HIPS, the extension ratio in the width direction remains nearly 1 but for materials with especially large shear deformation components, Λ_2 decreases significantly. In our experiments Λ_2 is measured from the

---

* The mass thickness is

$$\rho w = \left(\frac{\mu}{\rho}\right)^{-1} \cdot \mu w$$

where ρ is sample density, and (μ/ρ) is the weighted mean atomic mass absorption coefficient.

optical video images of the sample. The quantity Λ_3 is proportional to Λ_2 and is a function of sample geometry.

The strain due to crazing is determined from a calibrated conversion of the relative scattering invariant Q_{PIX} to the absolute scattering invariant $Q(Abs)$ as a function of time, viz.,

$$Q(Abs) = \frac{\Delta h}{\lambda_r^3} \frac{Q_{\mathrm{PIX}}}{j(PE, r)} \frac{I_t(PE, r)}{I_t(s, r)} V_{PE} \frac{\Delta a}{r^2} R_{PE} \quad (5)$$

where V_{PE} is the volume of the polyethylene (Lupolen) standard in the beam, r is the sample to detector distance, Δh is the pixel height in the vertical direction, $I_t(s, r)$ is the transmitted beam intensity through the sample for a specified time scan, $I_t(PE, r)$ is the transmitted beam intensity through the polyethylene standard for the same specified time scan, $j(PE, r)$ are the counts per pixel from the OMA for the intensity peak of the polyethylene standard, $\Delta a/r^2$ is the solid angle subtended by the detector element at distance r, and Δa is the area of each OMA detector element (i.e., one pixel) equal to $5 \times 10^{-4}\,\mathrm{cm}^2$. The peak intensity $I_t(PE, r)$ in Equation 5 is corrected for the finite width of the OMA slit and for the exposure time. The absolute calibration coefficient R_{PE}, which is also the Rayleigh factor, was found to be $5.95\,\mathrm{cm}^{-1}$ for the Lupolen standard. The uncorrected scattering invariant obtained from the Reticon/OMA is Q_{PIX}, expressed as,

$$Q_{PIX} = 2\pi \sum_{s_1}^{s_2} j(s_z) s_z \Delta s_z + Q_{Tail} \quad (6)$$

where s_z is the scattering vector equal to $(2 \sin \theta)/\lambda \cong 2\theta/\lambda$. In Equation 6 for Q_{PIX}, s_z is in "pixel" units, where each element on the OMA is one detector pixel and $\Delta s_z = 1$ in these units. The quantities s_1 and s_2 are the pixel at the top of the beam stop and the largest s_z read by the OMA, respectively. The quantity $I(s_z)$ is the number of counts obtained for the pixel at s_z from the OMA. The quantity Q_{Tail} is evaluated using Porod analysis as applied to scattering from crazes [18, 19] using the expression,

$$Q_{Tail} = 2\pi \int_{s_2}^{\infty} j(s_z) \cdot s_z \, ds_z = 2\pi \int_{s_2}^{\infty} \frac{K}{s_z^3} s_z \, ds_z = \frac{2\pi K}{s_2} = \frac{2\pi K}{P_{max}} \quad (7)$$

The quantity P_{max} is the scattering vector position of last pixel in the OMA scan. K is the Porod constant obtained from a Porod analysis (js_z^3 versus s_z) as discussed elsewhere [1, 19, 23].

The total volume of crazes in the X-ray beam $V_{Craze\ in\ beam}$ at a given instance in time is related to the absolute scattering invariant $Q(Abs)$ by the expression

$$V_{Craze\ in\ beam} = \frac{Q(Abs)}{(1 - \nu_f)\nu_F \sigma_T (\Delta\rho)^2} \quad (8)$$

The quantity ν_F is the average fibril volume fraction of the crazes as sampled by the X-ray beam, $\Delta\rho$ is the electron density difference between the matrix material and air, and σ_T is the Thomson electron scattering cross-section ($7.94 \times 10^{-26}\,\mathrm{cm}^2$). The values for ν_F are taken to be 0.25 and 0.37 for PS and SAN, respectively [2, 24].

Experimentally, the volume of crazes are measured in the volume $V_B(t)$ of material which is in the beam at time t. Assuming that there is an equal craze density in the region occupied by the beam and in the region now occupied by the original gauge volume V_0, the corresponding craze volumes in the two regions will be related by

$$d[V(t)_{Craze\ in\ gauge\ volume}] = d[V(t)_{Craze\ in\ beam} \Lambda_1 \Lambda_2] \quad (9)$$

so that the incremental true strain due to crazing is

$$d\varepsilon(t)_{CR} = \frac{d[V(t)_{Craze\ in\ beam} \Lambda_1(t) \Lambda_2(t)(1 - \nu_f)]}{V_0 \Lambda_1(t) \Lambda_2(t) \Lambda_3(t)} \quad (10)$$

By integration of Equation 10, the true craze strain can then be calculated from the scattering data, viz.

$$\varepsilon_{CR}(t) = \frac{(1 - \nu_f)}{V_0} \int_0^t \frac{d[V_{Craze\ in\ beam}(t) \Lambda_1(t) \Lambda_2(t)]}{\Lambda_1(t) \Lambda_2(t) \Lambda_3(t)} \quad (11)$$

where it is assumed that $(1 - \nu_f)$ is constant as a function of time during deformation and, thus, is removed from the integral. In practice, Equation 11 is integrated scan by scan to obtain the true crazing strain. The strain due to deformation events other than crazing (i.e., shear yield and rubber particle cavitation) is the "noncrazing" strain, ε_{NCR}, viz.,

$$\varepsilon_{NCR} = \varepsilon_T - \varepsilon_{CR} \quad (12)$$

The average craze fibril diameter, D, is obtained for a given scan having sufficient scattering intensity by using the expression

$$D = \frac{\lambda Q_{PIX}}{\pi^3 (1 - \nu_f) K} \left(\frac{\Delta h}{r} \right)^{-1} \quad (13)$$

in a manner discussed elsewhere [1, 19, 23].

3. Results

3.1. HIPS

Figs 5, 6, and 7 show the results from analysis of RTSAXS impact measurements on HIPS-1 at the average strain rates of about 7.1, 22.7, and $31.3\,\mathrm{s}^{-1}$, respectively. The times to fracture are, respectively, 73, 23, and 16 ms. The yield stresses for all three rates are about 3000 p.s.i. ($20.7\,\mathrm{MN\,m}^{-2}$). In each figure the changes in the total plastic strain, the plastic strain due to crazing, the non-craze plastic strain, the scattering centre size, and the nominal engineering stress are shown as a function of time. The scattering centre size is the average craze fibril diameter, which remains at about 14 nm, independent of the decade change in strain rate. This constancy with rate agrees with what has been previously reported for HIPS [1]. The previously reported craze fibril diameter is about 10 nm, the smaller value resulting from the effect of some detector saturation on the data analysis.

Fig. 8 shows the result of the analysis for HIPS-2 at the strain rate of $8.6\,\mathrm{s}^{-1}$. The only difference between HIPS-1 and HIPS-2 is the rubber gel particle size, 2.8 as opposed to 1.2 µm. As with HIPS-1, the deformation is dominated by non-craze deformation in very

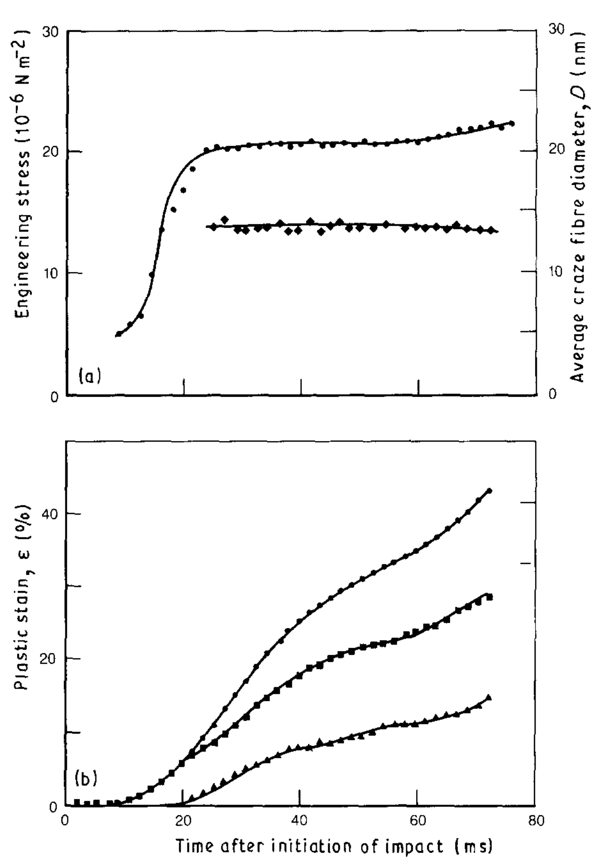

Figure 5 RTSAXS analysis of HIPS-1 at $7.1\ \mathrm{s}^{-1}$. (a) Plots of engineering stress and average craze fibril diameter (D) (◆). (b) Plots of total plastic strain (ε_T) (●), non-crazing strain (ε_{NCR}) (■), and strain due to crazing (ε_{CR}) (▲).

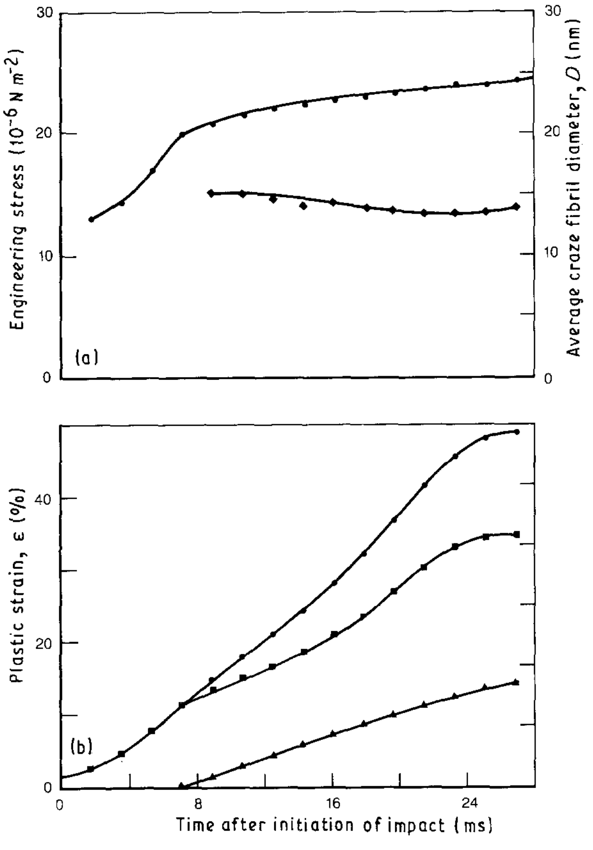

Figure 6 RTSAXS analysis of HIPS-1 at $22.7\ \mathrm{s}^{-1}$. The figure layout and labelling are identical to those of Fig. 5.

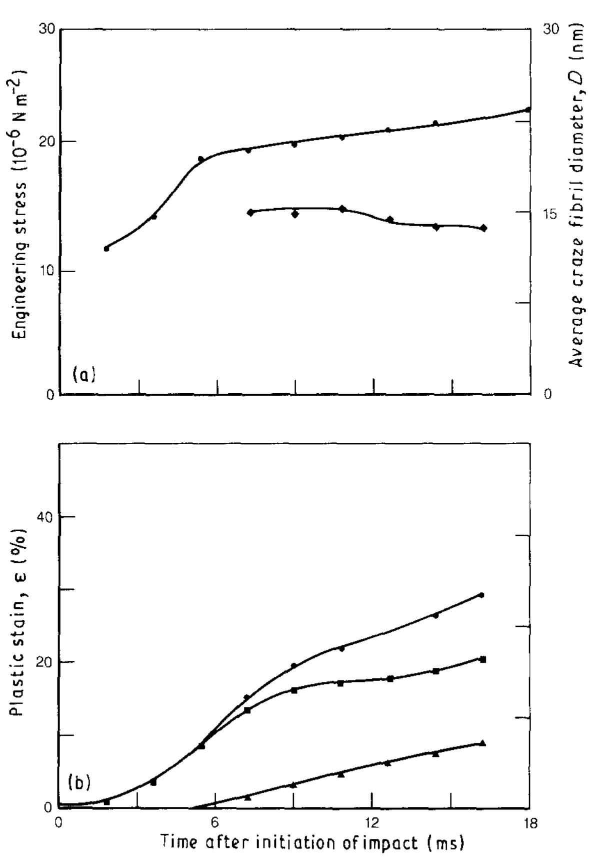

Figure 7 RTSAXS analysis of HIPS-1 at $31.3\ \mathrm{s}^{-1}$. The figure layout and labelling are identical to those of Fig. 5.

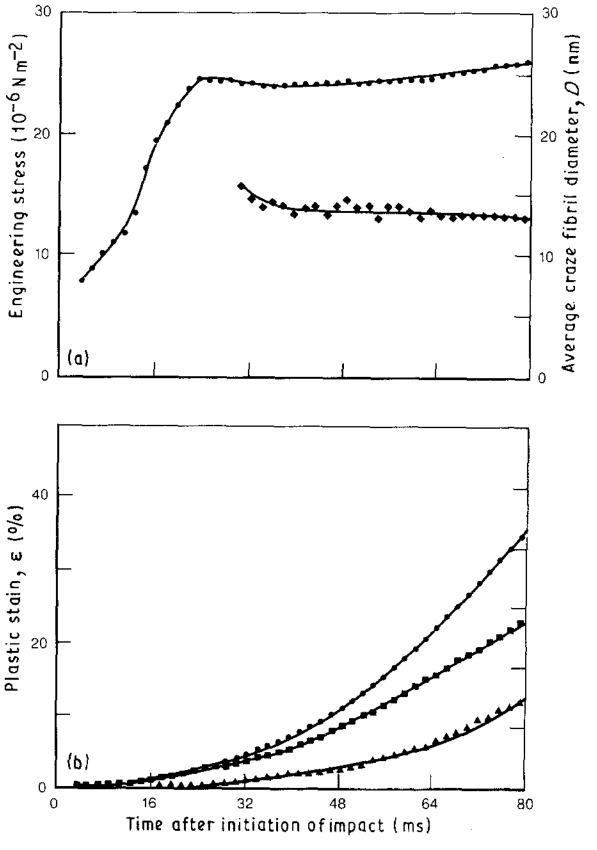

Figure 8 RTSAXS analysis of HIPS-2 at $8.6\ \mathrm{s}^{-1}$. The figure layout and labelling are identical to those of Fig. 5.

much the same proportion. A comparison of Figs 5 and 8 indicates that decreasing the particle size by half increases the yield stress from 3000 p.s.i. (20.7 MN m^{-2}) to 3300 p.s.i. (22.8 MN m^{-2}) and the lag time for crazing from about 19 to about 25 ms. The time to fracture increases slightly from 73 to 78 ms. The decrease in particle size also results in a decrease in per cent plastic strain at failure from roughly 45% to about 30%, in the tensile impact test at this relatively low rate. The craze fibril sizes are virtually identical for HIPS-1 and HIPS-2.

3.2. ABS

Examples of RTSAXS analyses for ABS-1 and ABS-2 at the deformation rates of 0.24 and 7.8 s^{-1}, respectively, are shown in Figs 9 and 10. The deformation character of ABS-1 is very much like that of the HIPS samples discussed previously, although the material is fairly brittle as indicated by its achieving only 11% strain at fracture. Increasing the rubber content from 10 to 22 wt % increases the strain at fracture to about 78%, as shown in Fig. 10 for ABS-2. The average craze fibril diameter for both samples is about 14 nm, once the scattering intensity from the craze fibrils is great enough to achieve good signal-to-noise ratio and valid analyses. Essentially no difference in craze fibril diameter is observed over the range in deformation rate explored for HIPS and ABS.

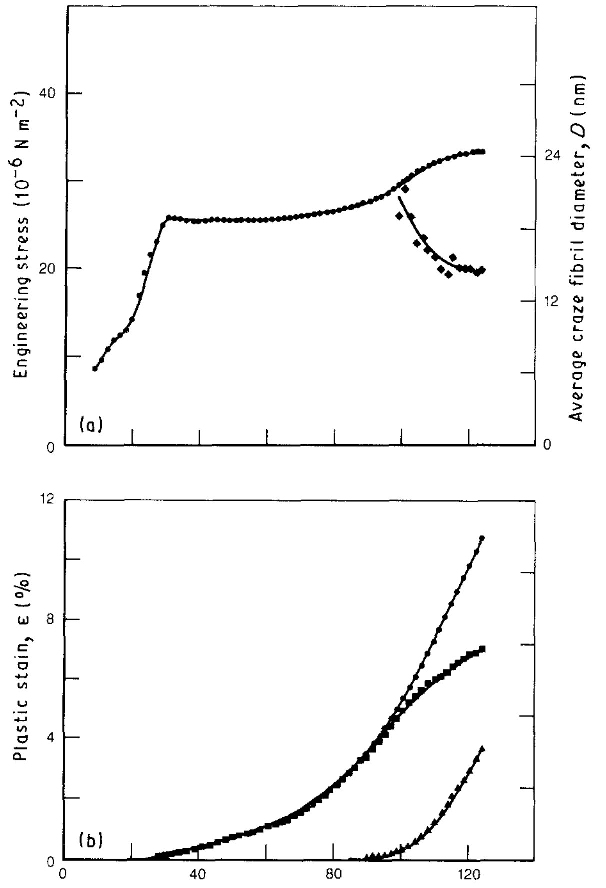

Figure 9 RTSAXS analysis of ABS-1 at 0.24 s^{-1}. The figure layout and labelling are identical to those of Fig. 5.

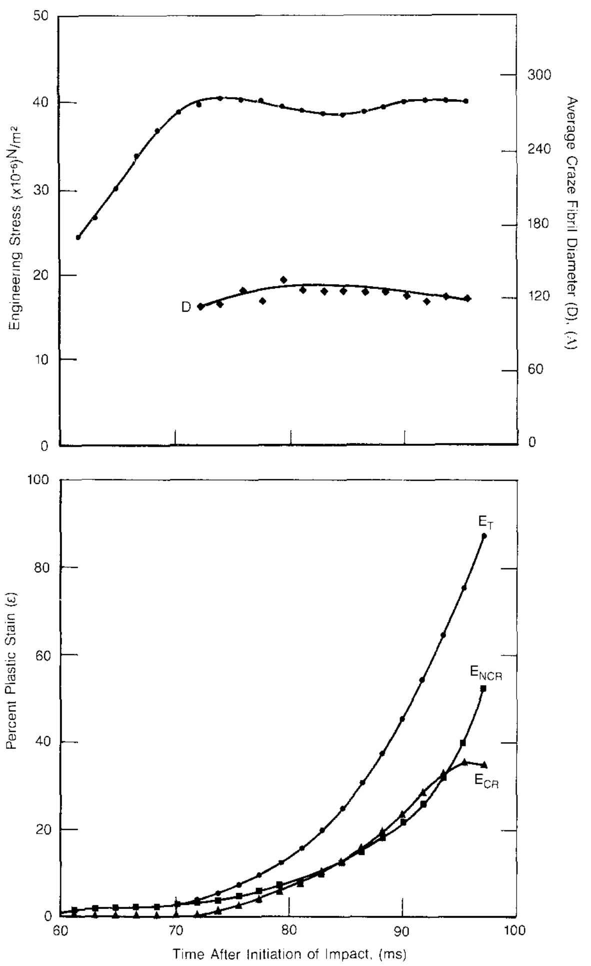

Figure 10 RTSAXS analysis of ABS-2 at 8.6 s^{-1}. The figure layout and labelling are identical to those of Fig. 5.

3.3. Polycarbonate–ABS Blends

The resulting series of line-summed intensities obtained from performing tensile impact RTSAXS experiments on PC–ABS-2 in the directions transverse and longitudinal to the direction of orientation are shown, respectively, in Figs 11 and 12. The nominal strain rates for these two runs are 18.5 and 26.7 s^{-1}. The time resolution between line-summed intensities is 1.82 ms $scan^{-1}$. Also shown for each case is a two-dimensional SAXS pattern obtained by video-based acquisition techniques described elsewhere [1, 2, 23] at the instant just before fracture. The small angle scattering pattern for these cases does not have the horizontal streak that results from the reflection from the top and bottom surfaces of well delineated crazes. (The circular beam stop in each case is somewhat off centre.) The scattering appears to be due to voids, but, as will be shortly discussed, is primarily due to localized and very irregular crazes in the SAN phase between the gel particles and the PC phase.

Figs 13 and 14 show the analyses for PC–ABS-2, for the experiments in which tensile direction was transverse and parallel to the direction of injection-moulded orientation, respectively. Figs 15 and 16 show the results of similar experiments for PC–ABS-1. A record is shown of only the later part of each of these runs for PC–ABS. The PC–ABS samples were often sufficiently strong to cause the miniature hydraulic tensile device to labour significantly. Despite

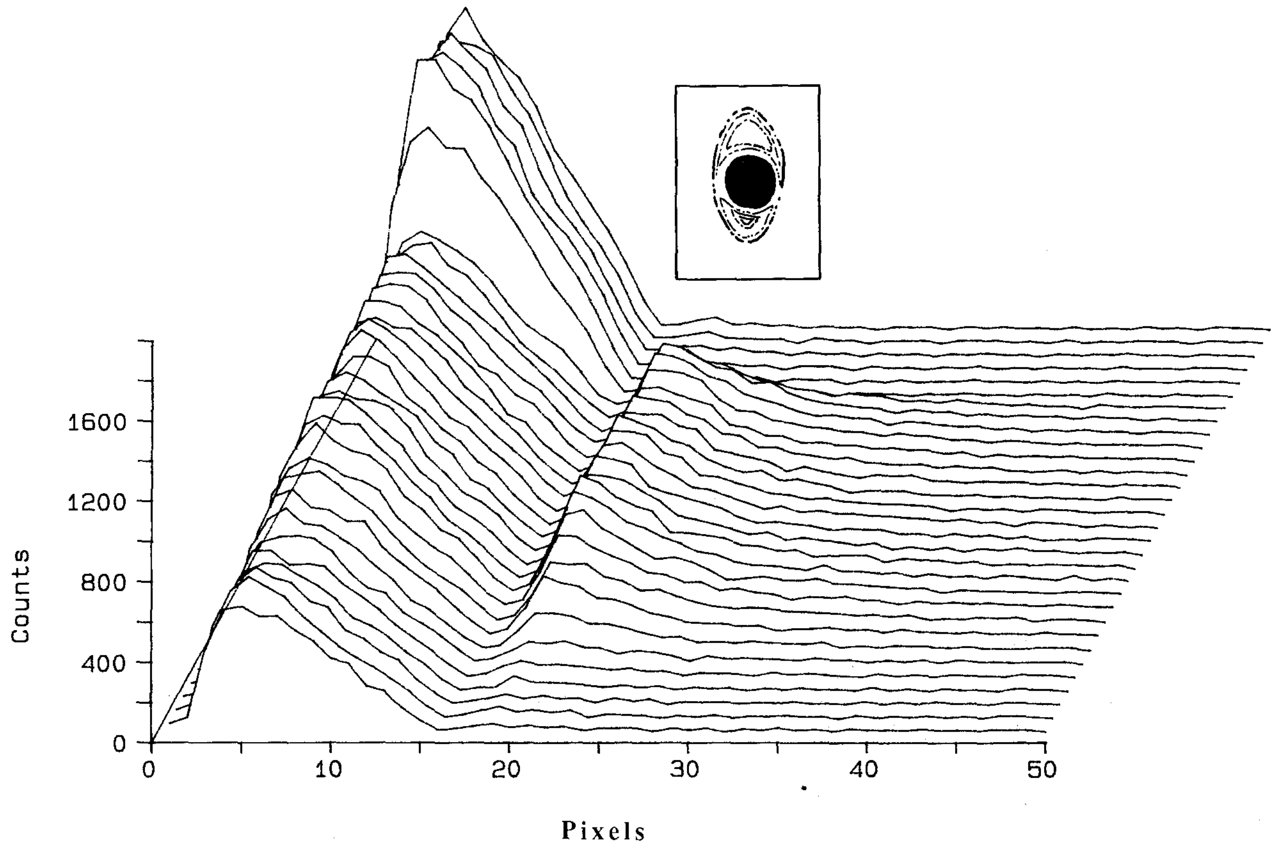

Figure 11 Line-summed intensities for RTSAXS during tensile impact of PC–ABS-2 in the direction transverse to the direction of orientation at a strain rate of 18.5 s^{-1}. Time resolution is 1.82 ms $scan^{-1}$. A typical two-dimensional SAXS pattern very near to fracture is shown in the inset.

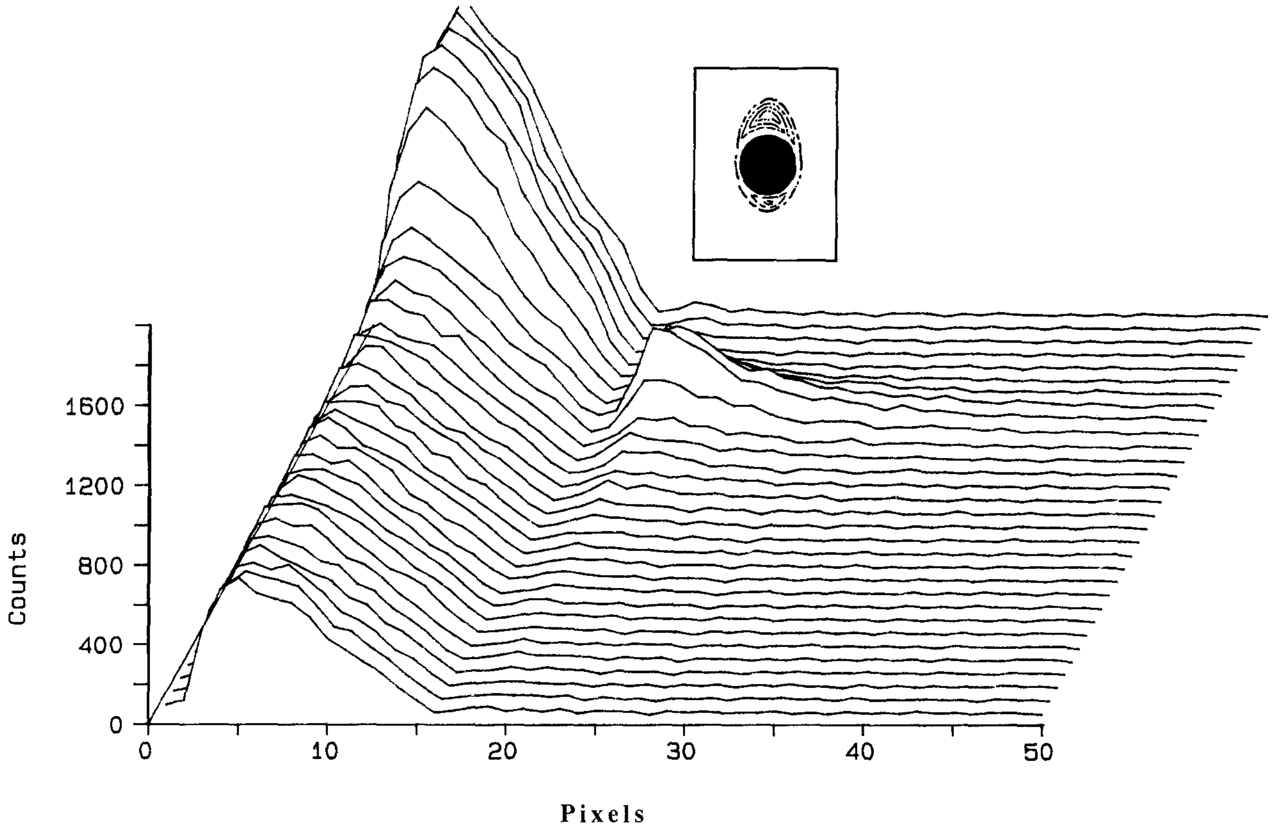

Figure 12 Line-summed intensities for RTSAXS during tensile impact of PC–ABS-2 in the direction parallel to the direction of orientation at a strain rate of 26.7 s^{-1}. Time resolution is 1.82 ms $scan^{-1}$. A typical two-dimensional SAXS pattern very near to fracture is shown in the inset.

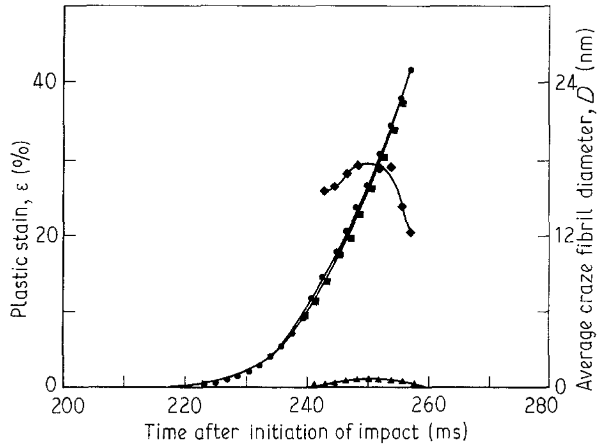

Figure 13 RTSAXS analysis of PC–ABS-2 in the transverse direction at a strain rate of 18.5 s^{-1} from 200 to 280 ms (● ε_T, ◆ D, ■ ε_{NCR}, ▲ ε_{CR}^{L}). Data are derived from Fig. 11.

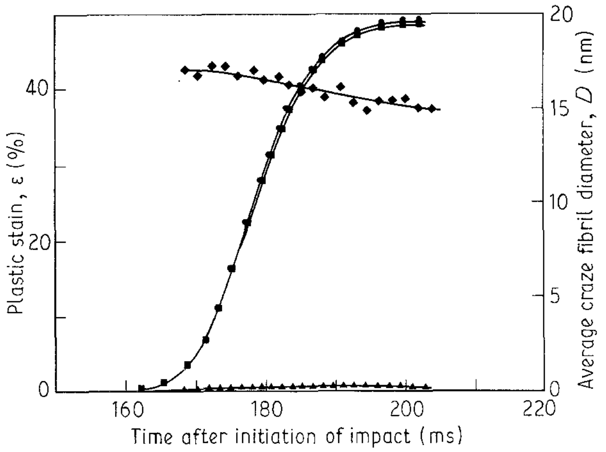

Figure 14 RTSAXS analysis of PC–ABS-2 in the parallel direction at a strain rate of 26.7 s^{-1} from 150 to 220 ms. Data are derived from Fig. 12.

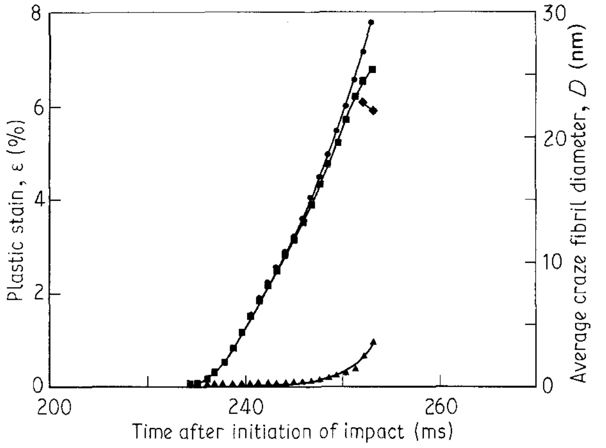

Figure 15 RTSAXS analysis of PC–ABS-1 in the transverse direction at a strain rate of 4 s^{-1} from 200 to 300 ms.

this handicap, nominal strain rates of 18.5, 26.7, 4, and 20 s^{-1} were achieved during plastic deformation, as shown, respectively, in Figs 13, 14 (PC–ABS-2), 15, and 16 (PC–ABS-1). The behaviour for the transverse orientation for PC–ABS-1 was sufficiently brittle with only 8% total plastic strain so that a strain rate of only 4 s^{-1} was obtained, which falls short of the values of about 20 s^{-1} for the other three cases.

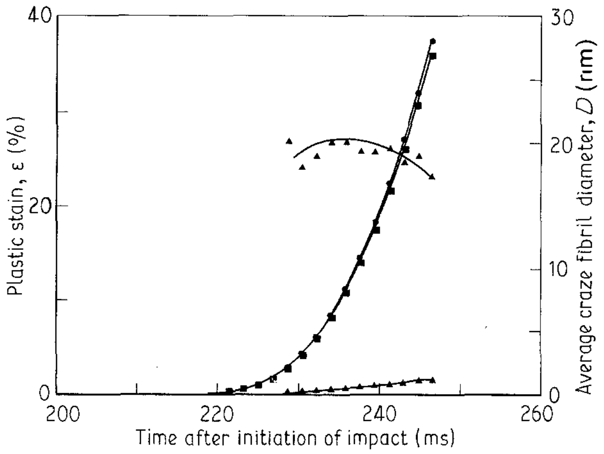

Figure 16 RTSAXS analysis of PC–ABS-1 in the parallel direction at a strain rate of 20 s^{-1} from 180 to 220 ms.

Although the scattering intensities obtained in these samples may be influenced by some nominal void scattering within the particles, the "lateness" of the scattering in the measured sequences suggest that the origin of the scattering is probably due to scattering from short crazes confined between the rubber particles and the PC phase in the SAN phase of the ABS. The scattering centre sizes for the PC–ABS samples range from 15 to 23 nm which is consistent with craze fibril diameter in SAN. If the scattering were associated primarily with scattering from voids within the rubber particles or voided particles as an aggregate, the scattering centre size would be expected to be significantly larger than 10 to 20 nm. This hypothesis that the SAXS comes from irregular crazes in the SAN phase is generally confirmed in the transmission electron photomicrograph shown in Fig. 17 of a deformed

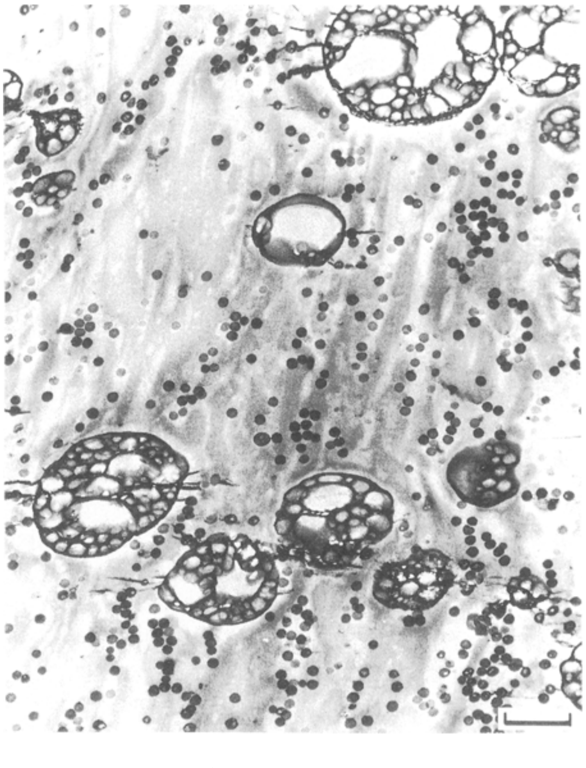

Figure 17 Transmission electron photomicrograph of a deformed PC–ABS blend. Marker length = 0.8 μm. Courtesy of B. H. Wooden and C. P. Bosnyak.

section of a PC–ABS blend. Many short crazes are to be seen primarily confined to relatively small SAN regions around the large gel rubber particles. The crazes are, of course, the precursor to actual fracture, suggesting that if the crazing could be suppressed, ductile elongation of the sample could be prolonged.

4. Discussion

Many analyses of dilatation during deformation of rubber-modified thermoplastics attribute most of the contribution to this part of the deformation to crazing [3, 5, 16]. In this light, the two most striking (and unexpected) results of the real-time X-ray analyses are: (1) the substantial increase in non-crazing plastic strain that precedes the onset of crazing, and (2) that the non-crazing strain is, in each instance, greater than that due to crazing. Our results are to be contrasted with scanning electron microscope observations of Gilbert and Donald [27] who found that a considerable portion of the strain ahead of a crack tip in HIPS was contributed, not by the crazes themselves but by the bending of glassy polymer "ligaments" between broken crazes. Here, since we find that the non-crazing strain largely precedes the crazing strain, this "broken craze" hypothesis for the origin of the non-crazing strain is not applicable. The most likely source of this non-crazing strain is the cavitation of rubber particles and the bending (plastic or elastic) of the glassy polymer "ligaments" between such particles. Our optical observations of the HIPS samples confirm previous observations that almost no change in sample lateral dimensions occurs prior to fracture, thus ruling out strain due to macroscopic shear. Shear deformation on a microscopic scale in the ligaments between cavitated rubber particles cannot be ruled out, however, by the absence of change in sample lateral dimensions.

Our results for ABS are consistent *in kind* with the observations made by Breuer *et al.* [25] for ABS materials. It has been previously observed that shear yield, presumably associated with particle cavitation, precedes crazing in ABS materials with relatively high impact strength [2, 25]. As with the HIPS samples, crazing occurs after the non-crazing strain is already large. However, with ABS, we believe that the non-crazing strain is most likely due to a combination of microscopic shear deformation between cavitated rubber particles (resulting in a change in the lateral sample dimension) and particle cavitation. Crazing never contributes to more than half of the total plastic strain associated with the deformation. The significant particle cavitation that is observed to precede crazing in both the HIPS and ABS systems studied here, means that the analyses of dilatation measurements during deformation of rubber-modified systems as practiced by Bucknall and others [3–16] are in need of re-evaluation.

The deformation of the PC–ABS blends selected here is heavily dominated by rubber particle cavitation in the ABS and the associated shear deformation in the PC. Crazing occurs typically at about 10 ms later for the direction parallel to the orientation, and about 20 ms later for the direction perpendicular to the orientation. The crazing makes up only a few per cent of the total plastic strain. Toughness is maximized when the axis of tension is parallel to the orientation direction and when the ABS component has a high rubber content. These results are consistent with general practical experience. The deformation event sequence and the types of deformation mechanisms, however, appear to be identical regardless of whether the samples are tested parallel or perpendicular to the orientation, and regardless of whether the rubber content in the ABS component is low or high. The principal difference is in the *amount* of particle cavitation and associated shear yield prior to fracture. In the parallel and perpendicular directions, the plastic strains at fracture for PC–ABS-1 are 36% and 8%, respectively. In the parallel and perpendicular directions, the plastic strains at fracture for PC–ABS-2 are 48% and 42%, respectively. The mechanical response of PC–ABS-1 is considerably more anisotropic than that of PC–ABS-2. The averaged plastic strains at fracture for PC–ABS-1 and PC–ABS-2 are 22% and 45% (in the ratio of 1:2), respectively. Given that the ABS rubber contents are 10% and 22% (in the ratio of 1:2.2), in that order for the two systems it can be concluded that the predominant role, by far, of the rubber particles is to provide manifold local sites of weakness via cavitation that permit the relaxation of triaxial tension and, thus, shear yielding on a massive scale.

5. Conclusions

The conclusions are as follows.

1. Real-time small-angle X-ray scattering has been shown to be a powerful technique that clearly delineates the sequence and types of deformation events, and their absolute contributions to the total plastic deformation in rubber-modified thermoplastic polymers. Samples of realistic thicknesses can be studied at high rates of deformation without the inherent limitations of microscopy and its requirement of thin samples (i.e., plane strain constraint is maintained on sample morphology).
2. Contrary to the conclusions of several previous dilatation-based studies, it has been demonstrated that non-crazing mechanisms, which we suspect are predominantly due to rubber particle cavitation and associated ligament bending of the surrounding glassy matrix occurs before crazing in HIPS and ABS. Crazing accounts for roughly only half of the total plastic strain in HIPS, and at most half in ABS materials. The proportion of plastic strain attributable to crazing can be much less than half the total in ductile ABS systems.
3. In HIPS or ABS systems, it appears that the amount of crazing strain at fracture decreases with increasing deformation rate, resulting in less toughness, but that the craze fibril diameter is roughly constant.
4. The predominant deformation mechanism in PC–ABS blends is shear in the PC with associated rubber gel particle cavitation in the ABS, thus there

appears to be a direct relationship between gel particle rubber content in the ABS and toughness of the blend. The mechanism is the same whether the tensile impact is in the direction parallel or perpendicular to the injection-moulded orientation. Crazing, although the precursor to final fracture, occurs after the predominant non-crazing mechanisms and contributes only a few per cent to the total plastic deformation.

Acknowledgements

We gratefully acknowledge the fellowship support of Donald Buckley, Jr., that was provided by The Dow Chemical Company. Thanks to B. H. Wooden and C. P. Bosnyak for permission to use the TEM photomicrograph in Fig. 17. The kind cooperation of the staff of the Cornell High Energy Synchrotron Source is gratefully acknowledged, and the use of the facilities of the Cornell Materials Science Center which is funded by the NSF-DMR-MRL program, is greatly appreciated.

References

1. R. A. BUBECK, J. A. BLAZY, E. J. KRAMER, D. J. BUCKLEY, Jr., and H. R. BROWN, *Polym. Commun.* **27** (1986) 357.
2. *Idem., Mater. Res. Soc. Symp. Proc.* **79** (1987) 293.
3. C. B. BUCKNALL and D. CLAYTON, *J. Mater. Sci.* **7** (1972) 202.
4. C. B. BUCKNALL, D. CLAYTON and W. E. KEAST, *ibid.* **7** (1972) 1443.
5. *Idem., ibid.* **8** (1973) 514.
6. C. B. BUCKNALL and I. C. DRINKWATER, *ibid.* **8** (1973) 1800.
7. C. B. BUCKNALL and W. W. STEVENS, *ibid.* **15** (1980) 2950.
8. C. B. BUCKNALL and C. J. PAGE, *J. Mater. Sci.* **17** (1982) 808.
9. C. B. BUCKNALL, I. K. PARTRIDGE and M. V. WARD, *ibid.* **19** (1984) 2064.
10. C. B. BUCKNALL and S. E. REDDOCK, *ibid.* **20** (1985) 1434.
11. C. B. BUCKNALL, F. F. P. COTE and I. K. PARTRIDGE, *ibid.* **21** (1986) 301.
12. C. B. BUCKNALL, P. DAVIES and I. K. PARTRIDGE, *ibid.* **21** (1986) 307.
13. *Idem, ibid.* **22** (1987) 1341.
14. C. B. BUCKNALL, "Toughened Plastics" (Applied Science, London 1977), Ch. 7 and 8.
15. C. B. BUCKNALL, C. J. PAGE and V. O. YOUNG, in "Toughness and Brittleness of Plastics", edited by R. D. Deanin and A. M. Crugnola (*Adv. Chem.* **154**) (American Chemical Society, Washington, DC, 1976) Ch. 15.
16. M. A. MAXWELL and A. F. YEE, *Polym. Engng Sci.* **21** (1981) 205.
17. P. J. FENELON and J. R. WILSON, *ibid.* **15,** Ch. 20.
18. E. PARADES and E. W. FISCHER, *Makromol. Chem.* **180** (1979) 2707.
19. H. R. BROWN and E. J. KRAMER, *J. Macromol. Sci.-Phys.,* **19B** (1981) 487.
20. D. J. BUCKLEY, Jr., E. J. KRAMER, R. A. BUBECK and H. R. BROWN, to be submitted for publication.
21. E. R. MOORE, ed., in "Encyclopedia of Polymer Engineering and Science", 2nd Edn, Vol. 16 (John Wiley, Chichester, 1989) pp. 1–246.
22. H.-J. SUE and A. F. YEE, *J. Mater. Sci.* **24** (1989) 1447.
23. P. J. MILLS, H. R. BROWN and E. J. KRAMER, *ibid.* **20** (1985) 4413.
24. A. M. DONALD and E. J. KRAMER, *ibid.* **17** (1982) 1871.
25. H. BREUER, J. STABENOW and F. HAAF, International Conference on Toughened Plastics (Plastics and Rubber Institute, London, 1978) Paper 13.
26. R. A. BUBECK and D. J. MOLL, Unpublished results.
27. D. G. GILBERT and A. M. DONALD, *J. Mater. Sci.* **21** (1986) 1819.

Received 19 June
and accepted 3 July 1990